Multi-Responsive Thermally Activated Delayed Fluorescence Materials: Optical $ZnCl_2$ Sensors and Efficient Green to Deep-red OLEDs

Changfeng Si,[a‡] Abhishek Kumar Gupta,[a,b‡] Biju Basumatary,[a] Aidan P. McKay,[a] David B. Cordes,[a] Alexandra M. Z. Slawin,[a] Ifor D. W. Samuel,[b*] and Eli Zysman-Colman[a*]

[a] Organic Semiconductor Centre, EaStCHEM School of Chemistry, University of St Andrews, St Andrews, Fife, UK. KY16 9ST, Fax: +44-1334 463808; Tel: +44-1334 463826

[b] Organic Semiconductor Centre, SUPA School of Physics and Astronomy, University of St Andrews, St Andrews, Fife, UK. KY16 9SS, Fax: +44-1334 463808; Tel: +44-1334 463826

Corresponding: eli.zysman-colman@st-andrews.ac.uk; idws@st-andrews.ac.uk

[‡] equal contributions

Key words: Deep red emitters, TADF, dibenzo[a,c]phenazine, $ZnCl_2$ sensor, organic light-emitting diode

Abstract

Thermally activated delayed fluorescence (TADF) is an emission mechanism whereby both singlet and triplet excitons can be harvested to produce light. Significant attention has been devoted to developing TADF materials for organic light-emitting diodes (OLEDs), while their use in other organic electronics applications such as sensors, has lagged. We have developed and systematically studied a family of TADF emitters, **TPAPyAP**, **TPAPyBP**, and **TPAPyBPN** containing a triphenylamine (TPA) donor and differing nitrogen-containing heterocyclic pyrazine-based acceptors. Depending on the acceptor strength, these three compounds emit with photoluminescence maxima (λ_{PL}), of 516 nm, 550 nm, and 575 nm in toluene. Notably, all three compounds showed a strong and selective spectral response to the presence of $ZnCl_2$, making them the first optical TADF sensors for this analyte. We also demonstrate that these three emitters can be used in vacuum-deposited OLEDs, which showed moderate efficiencies. Of note, the device with **TPAPyBPN** in 2,8-bis(diphenyl-phoshporyl)-dibenzo[b,d]thiophene (PPT) host emitted at 657 nm and showed an EQE_{max} 12.5%. This electroluminescence was significantly red-shifted yet

showing comparable efficiency compared to a device fabricated in 4,4′-bis(*N*-carbazolyl)-1,1′-biphenyl (CBP) host (λ_{EL}= 596 nm, EQE_{max} = 13.6%).

Introduction

Optical sensors are widely used in many applications, including in telecommunications, environmental monitoring, industrial automation, and medical devices.[1–4] An important class of optical sensors uses fluorescent compounds as the basis for their detection mechanism thanks to their numerous benefits including high specificity, low detection limits, fast response time, and technical simplicity.[5] Fluorescent sensors typically work by exhibiting a change in their emission, such as fluorescence intensity, emission wavelength or lifetime, in response to interactions with specific analytes or environmental changes.[6,7] Organic fluorescent compounds such as rhodamines,[8,9] fluoresceins[10], cyanine,[11] BODIPY,[12,13] and coumarin dyes[14] have long been used in optical sensing. Phosphorescent complexes have also been explored as sensors in oxygen sensing,[15] metal ion detection,[16] biomolecule detection,[17] and temperature sensing.[18] Indeed, both oxygen and temperature sensing rely in particular on accessible triplet excited states of the sensor.

Thermally activated delayed fluorescence (TADF) emitters are a class of emissive compounds that have small singlet-triplet excited state energy gaps (ΔE_{ST}).[19–21] They have garnered much attention due to their capacity to harvest both singlet and triplet excitons to produce light in electroluminescent devices such as organic light-emitting diodes (OLEDs).[20,21] They have increasingly been used in other applications, most notably as photocatalysts and as bioimaging reagents.[22–24] However, very few reports exist documenting the use of organic TADF materials as sensors.[25–27] The first reported example employed a TADF compound, acridine yellow (Figure **1a**), as a temperature sensor.[28] Steinegger *et al.* subsequently reported a series of carbazole-substituted dicyanobenzene and diphenylamine-substituted anthraquinone donor-acceptor (D-A) TADF emitters, such as compound **a3** (Figure **1a**), for use as oxygen and temperature sensors.[29] In doped films, these dyes exhibit a temperature sensitivity in the investigated temperature range (278–323 K), showing a 1.4 to 3.7% K^{-1} change of the delayed lifetime, compared to that at 298 K.[29] Tonge *et al.* disclosed a TADF polymer, **PTZ-ODA** (Figure **1a**), which acts as a single-component ratiometric oxygen sensor.[30] In addition to oxygen and temperature sensors, Li *et al.*
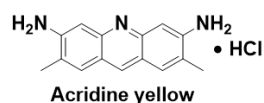
2

developed a sensor for solvent polarity based on compound **3** (Figure **1b**), which shows dual emissions at 332 nm (strong LE fluorescence) and 435 nm (weak CT TADF) in DCM under air. Using the solvent-invariant LE fluorescence as an internal reference, the ratio of the intensities of the LE and CT bands as well as the ratios of the prompt and delayed emission lifetimes were used to calibrate against solvent polarity.[31] Recently, Yin *et al.* reported a TADF turn-on chemosensor, **DCF-MPYM-lev** (Figure **1c**), for sulfite ion SO_3^{2-} detection. The fluorescence intensity of **DCM-MPYM-lev** solution in CH_3CN/PBS buffer (1/1) significantly increased and dual emissions at 535 nm and 640 nm were observed after the addition of SO_3^{2-}. **DCF-MPYM-lev** was also used to monitor exogenous SO_3^{2-} in living cells.[32] Qiu *et al.* reported the carbazole-triazine-based donor-acceptor TADF emitter **PhTRZ-OCHO** (Figure **1c**) as a fluorescence turn-off/fluorescence quenching sensor for the detection of Na^+, Mg^{2+} and Fe^{3+} ions.[26] The emission intensity at 470 nm of **PhTRZ-OCHO** decreased on the addition of many of the metal ions tested (Ba^+, Ca^+, Cd^{2+}, Co^{2+}, Cr^{2+}, Cu^{2+}, Fe^{3+}, Hg^{2+}, K^+, Mg^{2+}, Mn^{2+}, Na^+, Ni^{2+}, Pb^+), the strongest emission quenching occurred in the presence of Na^+, Mg^{2+} and Fe^{3+}. The remarkable fluorescence quenching behavior was attributed to the metal-binding aldehyde group present in **PhTRZ-OCHO** where, in the presence of these ions, the charge transfer (CT) state is destabilized and non-emissive.

$ZnCl_2$ is a versatile Lewis acid used widely in chemical manufacturing as a dehydrating agent, catalyst, and in materials preparation..[33] $ZnCl_2$ is also used in the textile industry as a mordant. Monitoring its levels is essential for both industrial process control and environmental regulation.[34] Additionally, while zinc is vital for biological processes, $ZnCl_2$ can be toxic and corrosive at high concentrations, making it important to monitor its presence for public health and safety reasons.[35] Although there are plenty of studies on the detection of Zn^{2+}, motivated by its importance in various biological processes,[36,37] there have been few reports of an optical sensor specifically designed for the detection of $ZnCl_2$. Manandhar *et al.* reported a pyrene-based triazole receptor (**pyrene-derived molecule**), which formed self-assembled induced excimers upon the addition of $ZnCl_2$. The **Pyrene-derived molecule** showed two distinct emission bands emanating from monomers and excimers.[38] This compound, however, provided a spectral response for other Zn^{2+} salts and was not specific for the detection of $ZnCl_2$. Sabarinathan *et al.* reported selective colorimetric sensing of $ZnCl_2 \cdot 2H_2O$ by the polyoxometalate–salt (**POM-salt**).[39] The addition of $ZnCl_2 \cdot 2H_2O$ into a mixture of **POM-salt** in DMSO–H_2O resulted in the formation of blue color;
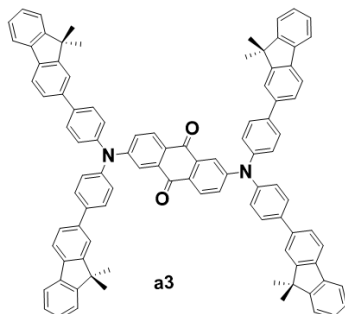
3

notably, anhydrous $ZnCl_2$ did not produce the color change under the same conditions. To the best of our knowledge, these are the only two optical sensors for $ZnCl_2$ that have been reported to date.

Here, we report three new TADF donor-acceptor emitters with a triphenylamine (TPA) donor and nitrogen-containing heterocyclic pyrazine-based acceptor, 4-(acenaphtho[1,2-b]pyrido[2,3-e]pyrazin-10-yl)-*N,N*-diphenylaniline (**TPAPyAP**), 4-(dibenzo[*f,h*]pyrido[2,3-b]quinoxalin-12-yl)-*N,N*-diphenylaniline (**TPAPyBP**) and *N,N*-diphenyl-4-(pyrido[2',3':5,6]pyrazino[2,3-*f*][1,10]phenanthrolin-12-yl)aniline (**TPAPyBPN**) (Figure **1d**). Theoretical and experimental results demonstrate that the electron-withdrawing strength of the acceptor increases with both the increased conjugation of the acceptor and the number of nitrogen atoms contained within, leading to a red-shift of the emission within the series. These nitrogen atoms can also act as ligands for metal binding and the resulting change in photophysics can be exploited in metal ion sensing.[40] We found that these compounds exhibited a stark spectral response to the detection of $ZnCl_2$, due to the formation of zinc chlorido complexes. Of these three emitters, **TPAPyBP** showed the most dramatic and fast fluorescence response toward $ZnCl_2$ by shifting emission from green (550 nm) to deep red (680 nm). We separately explored these compounds as emitters in OLEDs and documented a rather large host polarity-induced shift in the emission from films doped in 4,4′-bis(N-carbazolyl)-1,1′-biphenyl (CBP) to 2,8-bis(diphenyl-phosphoryl)-dibenzo[b,d]thiophene (PPT). In particular, the OLEDs with **TPAPyBPN** in PPT emitted at 657 nm and showed an EQE_{max} 12.5%. This electroluminescence was 61 nm red-shifted in comparison to a device fabricated in CBP host (λ_{EL}= 596 nm, EQE_{max} = 13.6%), without significant loss in efficiency. The devices with **TPAPyAP** and **TPAPyBP** doped in CBP emitted at λ_{EL}= 526 nm with EQE_{max} = 7.6% and λ_{EL}= 558 nm with EQE_{max} = 9.1%, respectively.

Figure **1**. Reported TADF emitters' structures for (a) temperature and oxygen sensors; (b) environmental polarity sensors; (c) anion and cation sensing; (d) fluorescent sensor for Zn^{2+} ions; (e) This work: Multi-responsive TADF emitters based on planar and rich N-type acceptors.
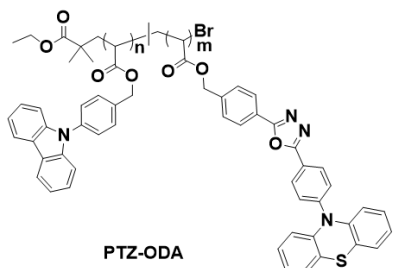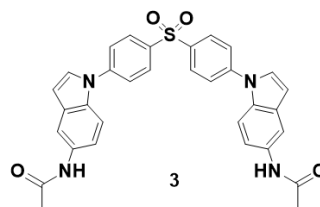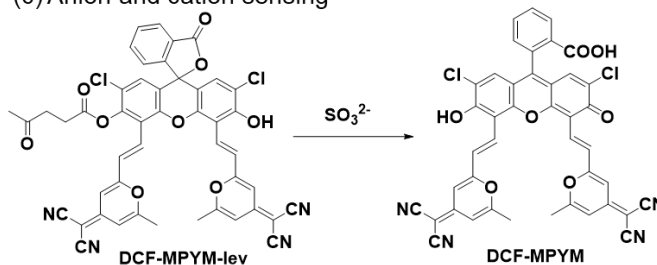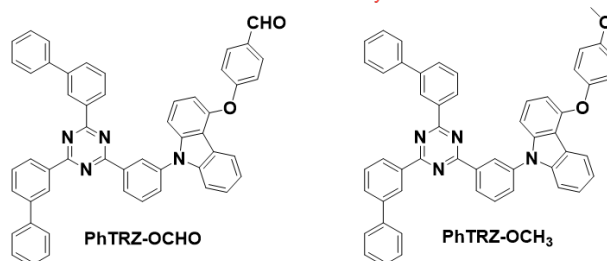
5

Results and Discussion

Synthesis and Characterization

The synthesis of the family of **TPAPyX** (X = AP, BP, BPN) emitters follows a common route (Scheme **1**). Intermediate 5-(4-(diphenylamino)phenyl)pyridine-2,3-diamine, **1**, was obtained via a Suzuki-Miyaura cross-coupling of *N,N*-diphenyl-4-(4,4,5,5-tetramethyl-1,3,2-dioxaborolan-2-yl)aniline and 5-bromopyridine-2,3-diam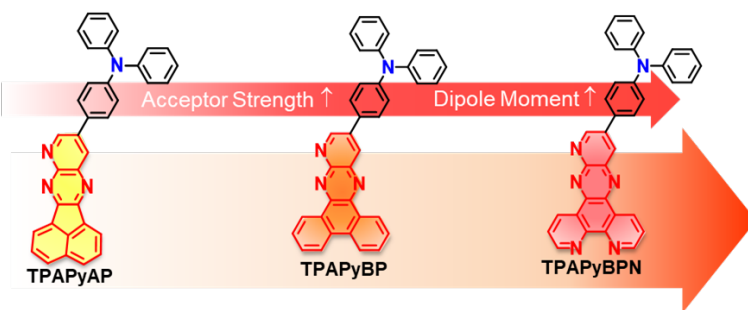ine in 84% yield. The target compounds **TPAPyAP**, **TPAPyBP** and **TPAPyBPN** were each obtained in high yield through a condensation between **1** and the corresponding α-diketones; acenaphthylene-1,2-dione (AP), phenanthrene-9,10-dione (BP) and 1,10-phenanthroline-5,6-dione (BPN), respectively. The identity and purity of the three emitters were verified using a combination of ^{1}H NMR, ^{13}C NMR spectroscopy, melting point determination, high-resolution mass spectrometry, elemental analysis, single crystal X-ray diffraction studies, and high-performance liquid chromatography (Figures **S1-S13**).
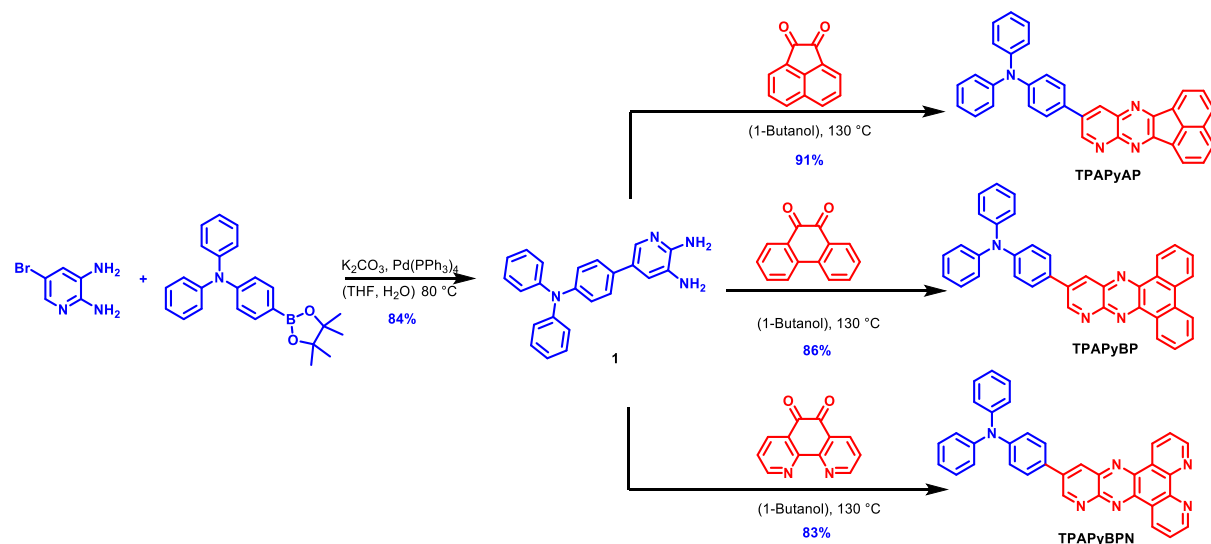
Scheme **1.** Synthesis of **TPAPyAP**, **TPAPyBP** and **TPAPyBPN**.

X-Ray diffraction analysis of TPAPyBP and TPAPyBPN

Single crystals of **TPAPyBP** and **TPAPyBPN** were obtained by slow evaporation of a saturated toluene solution at room temperature. The structure and packing mode of both molecules in the solid state are shown in Figure **2** and the crystallographic data are shown in Table **S1**. The

6

phenylene bridge is near coplanar with the adjacent ring of the acceptor in both compounds, except in one independent molecule of **TPAPyBP**, where it is more noticeably out of plane (**TPAPyBP**: 2.79 (Figure **2a**) and 31.03° (Figure **S14a**), **TPAPyBPN**: 4.36° (Figure **2b**)). **TPAPyBP** packs as arrays of co-planar compounds along the *b*-axis, the donor groups of alternate molecules oriented to opposite sides to avoid steric clash. These arrays are held together by slipped π–π stacking interactions, with adjacent molecules 3.24 and 3.49 Å apart, centroid···centroid distances of 3.522(2) to 3.753(2) Å (Figures **2a** and **S14**). In addition to these, CH···π interactions occur both to help further link adjacent molecules within the stacks (H···centroid distances of 2.78 Å), and also to link adjacent stacks together (two independent H···centroid distances of 2.92 Å). **TPAPyBPN**, also adopts a π-stacked arrangement, however, these arrays form along the *a*-axis, and adjacent molecules adopt an alternating head-to-tail packing pattern. Adjacent molecules are separated by 3.36 Å, with centroid···centroid distances of 3.7149(17) to 3.7901(16) Å (Figures **2b** and **S15**). Along the *a*-axis there are also C–H···N hydrogen bonds present (2.54 Å) that link adjacent molecules in the π-stacked arrays (Figures **2b**). Additional CH···π interactions (H···centroid distances of 2.81 and 2.92 Å) occur between adjacent stacks and help to stabilize the packing.
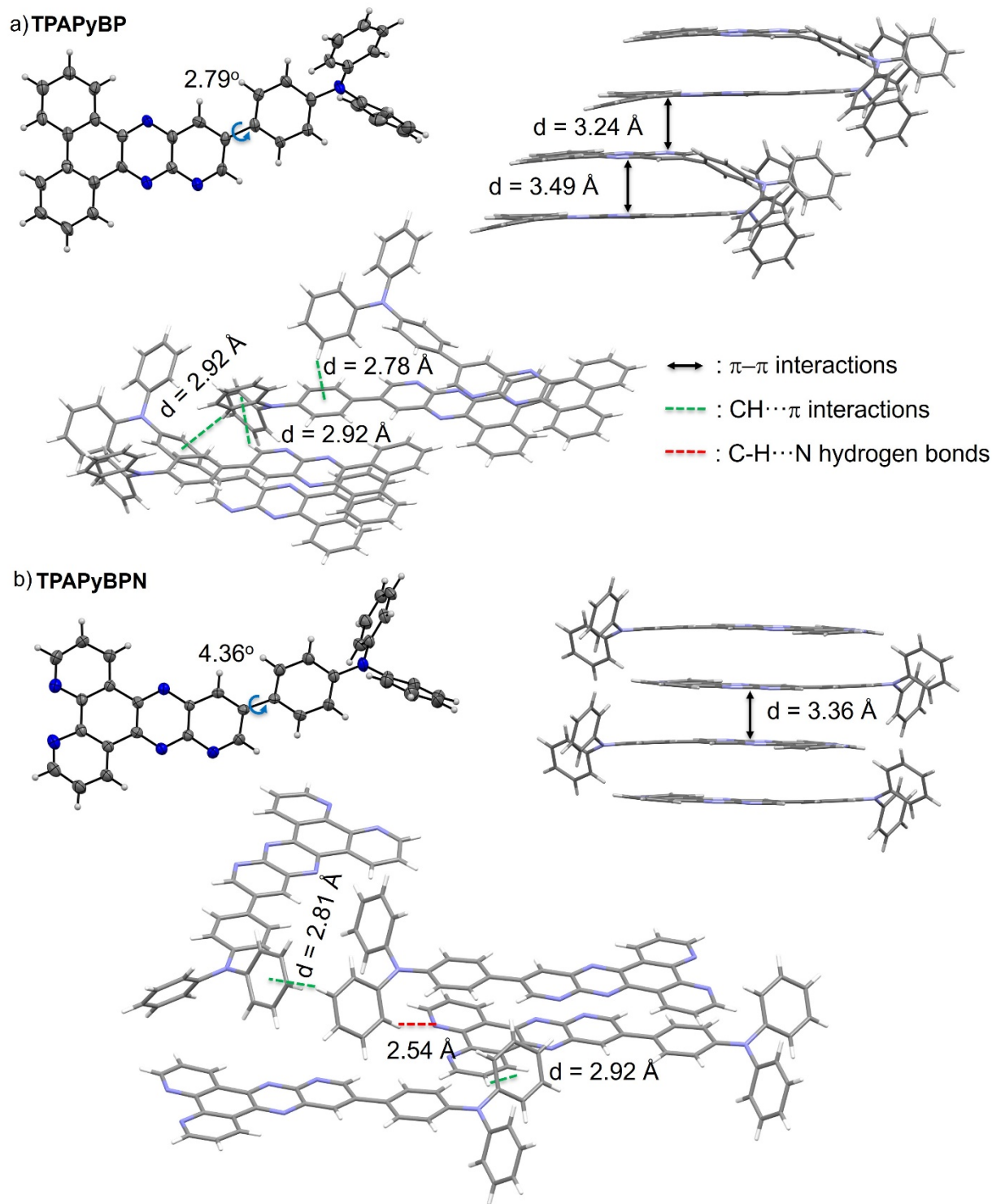
7

Figure **2**. Thermal ellipsoid plot (ellipsoids are drawn at the 50% probability level), view of the spacing between adjacent π-stacked molecules, and view showing interactions between adjacent

8

molecules of (a) **TPAPyBP** (only one independent molecule shown in the ellipsoid plot) and (b) **TPAPyBPN**, respectively.

Theoretical Calculations

The ground-state (S_0) geometries of **TPAPyAP, TPAPyBP and TPAPyBPN** were optimized using density functional theory (DFT) at the PBE0[41]/6-31G(d,p)[42] level of theory in the gas phase starting from a geometry generated in Chem3D.[43] At the optimized S_0 geometries, the dihedral angles between the bridging phenylene of the TPA and acceptor moieties are around 31º for **TPAPyAP**, 39º for **TPAPyBP** and 41º for **TPAPyBPN** (Figure **S16**), slightly larger than those found in the crystal structures of the latter two (Figure **2**). The calculated energy levels of the highest occupied molecular orbitals (HOMOs) and lowest unoccupied molecular orbitals (LUMOs) are shown in Figure **3** and **S17** and the results are summarized in Table **S2**. The HOMOs are localized on the TPA donor, with some minor contribution onto the proximal pyridine ring of the acceptor moiety. The LUMOs of all three compounds are localized on the acceptor group, with some contribution also located on the bridging phenylene of the TPA donor. As the acceptor strength increases along the series from **TPAPyAP** to **TPAPyBP** and **TPAPyBPN** both the HOMO and LUMO are stabilized, with the stabilization more significant for the latter. The HOMO-LUMO gap, $\Delta E_{\text{HOMO-LUMO}}$, thus decreases from 3.21 eV for **TPAPyAP** to 3.00 eV for **TPAPyBP** and 2.90 eV for **TPAPyBPN** (Figure **3a**). The excited-state properties were calculated using time-dependent density functional theory (TD-DFT) within the Tamm-Dancoff approximation (TDA-DFT) based on the optimized ground-state geometries.[44,45] The oscillator strength, *f*, for the $S_0{\rightarrow}S_1$ transition is high at 0.47, 0.39 and 0.36 for **TPAPyAP, TPAPyBP** and **TPAPyBPN**, respectively, reflecting a significant overlap of the electron density between the HOMO and LUMO, a result of the relatively small torsions that exist between the TPA and the acceptor moieties. The S_1 energies are 2.82 eV for **TPAPyAP** to 2.59 eV for **TPAPyBP** and 2.48 eV for **TPAPyBPN**, while the T_1 energies likewise decrease from 2.44 eV, 2.25 eV, and 2.17 eV, respectively, following a similar trend to that observed for $\Delta E_{\text{HOMO-LUMO}}$. The degree of spatial separation of the frontier orbitals in **TPAPyBPN** is reflected in a ΔE_{ST} of 0.31 eV, while the larger overlap between HOMO and LUMO for **TPAPyAP** and **TPAPyBP** lead to ΔE_{ST} values that are slightly larger at 0.37 eV and 0.34 eV, respectively.

9

Natural transition orbital (NTO) analyses at the optimized S_1 and T_1 geometries calculated at the TDA-DFT-PBE0/6-31G(d,p) level are shown in Figures **3c** and **3d**, respectively. For all three compounds, the S_1 states are of charge transfer (CT) character from the TPA donor to the acceptor. However, the T_1 states possess mixed CT and locally excited (LE) character on the acceptor. At the relaxed S_1 geometry, there is a decreasing S_1 -T_1 spin-orbit coupling matrix element (SOCME) from 0.27 cm^{-1} in **TPAPyAP** to 0.21 cm^{-1} in **TPAPyBP** and 0.16 cm^{-1} in **TPAPyBPN** (Figure **3a**), while at the relaxed T_1 geometry, the T_1 -S_1 SOCME are 0.17, 0.22, 0.22 cm^{-1} for **TPAPyAP**, **TPAPyBP** and **TPAPyBPN**, respectively.

10
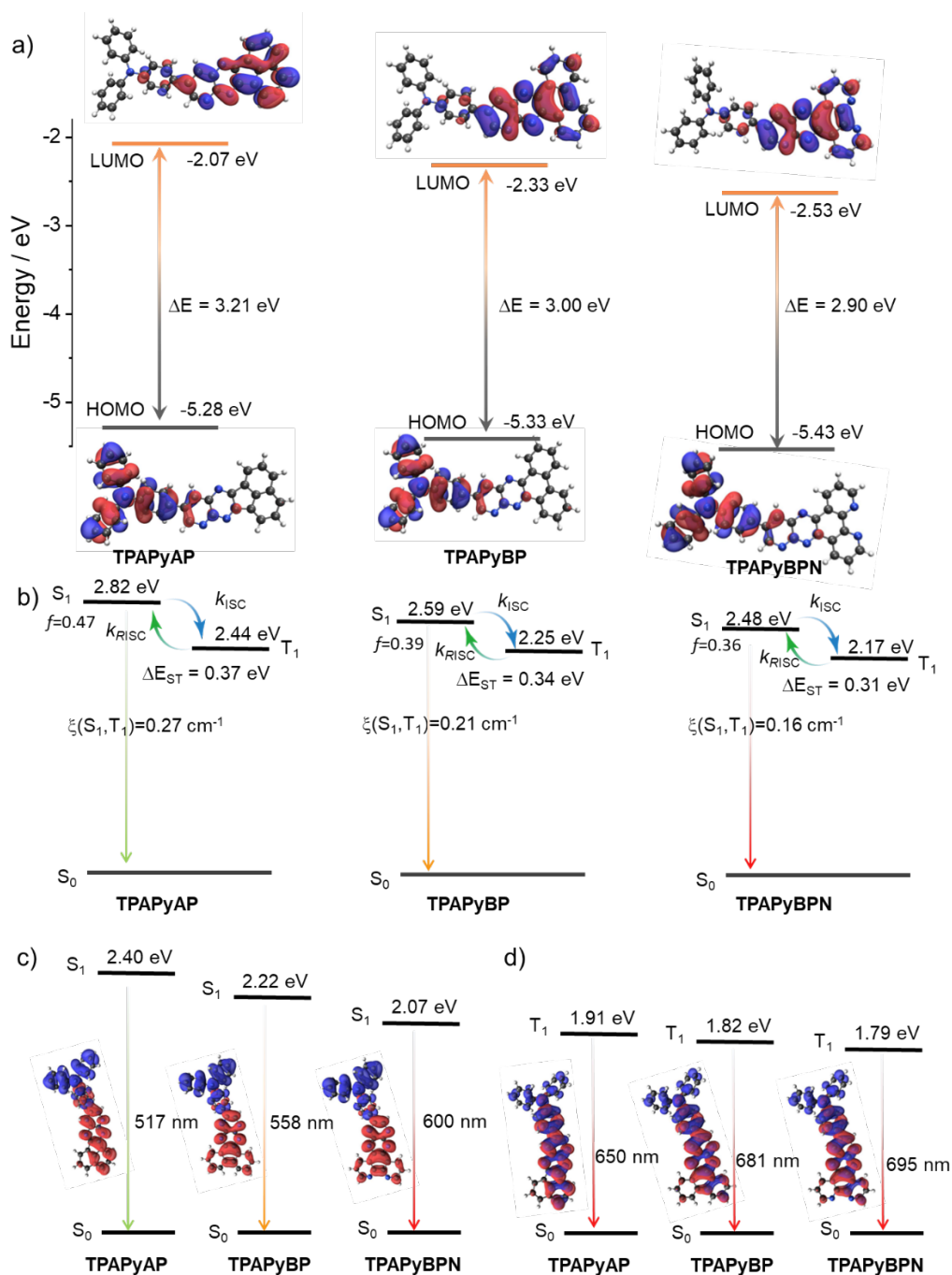
Figure **3**. (a) Frontier molecular orbitals (isovalue: 0.02) and (b) vertical excitation energy levels of **TPAPyAP, TPAPyBP** and **TPAPyBPN** calculated using the optimized S_0 geometry in the gas phase at the PBE0/6-31G(d,p) level. c) S_1 electron density distributions (isovalue: 0.02) and S_1 vertical emission energies calculated in the gas phase at the S_1 optimized geometry at the TDA-DFT PBE0/6-31G(d,p) level. d) T_1 electron density distributions (isovalue: 0.02) and T_1 vertical

emission energies calculated in the gas phase at the T_1 optimized geometry at the TDA-DFT PBE0/6-31G(d,p) level (hole (blue) & electron (red)).

Electrochemistry

The electrochemical behavior of **TPAPyAP, TPAPyBP** and **TPAPyBPN** was studied by cyclic voltammetry (CV) and differential pulse voltammetry (DPV) in degassed dichloromethane (DCM) with tetra-*n*-butylammonium hexafluorophosphate ([^{n}Bu$_4$N]PF$_6$) as the supporting electrolyte. Voltammograms are referenced versus F_c/F_c^+ and the data are reported versus a saturated calomel electrode (SCE) and collated in Table **S3.** As shown in Figure **4a**, all three compounds show reversible oxidation and reduction processes. The E_{red}, determined from the DPV peak values, are -1.39 (**TPAPyAP**), -1.21 V (**TPAPyBP**) and -1.09 V (**TPAPyBPN**), respectively, reflecting the expected anodic shift that is mirrored in the trend of calculated stabilized LUMO levels (Figure **S18**) due to the increasing π-accepting ability of the acceptor units from AP < BP < BPN. The corresponding LUMO levels are −2.95 eV, −3.13 eV and −3.25 eV for **TPAPyAP, TPAPyBP** and **TPAPyBPN**, respectively. All three emitters possess similar oxidation potentials (E_{ox} = 1.01 V for **TPAPyAP**, 1.00 V for **TPAPyBP** and 1.02 V for **TPAPyBPN**) due to the use of the same TPA donor unit. The HOMO levels of **TPAPyAP, TPAPyBP** and **TPAPyBPN** are −5.33, −5.35 and −5.35 eV, respectively. The HOMO–LUMO gaps for **TPAPyAP, TPAPyBP** and **TPAPyBPN** are thus 2.38, 2.22 and 2.10 eV, respectively, which mirror the trend in the DFT calculated values of 2.79, 2.62, 2.46 eV.
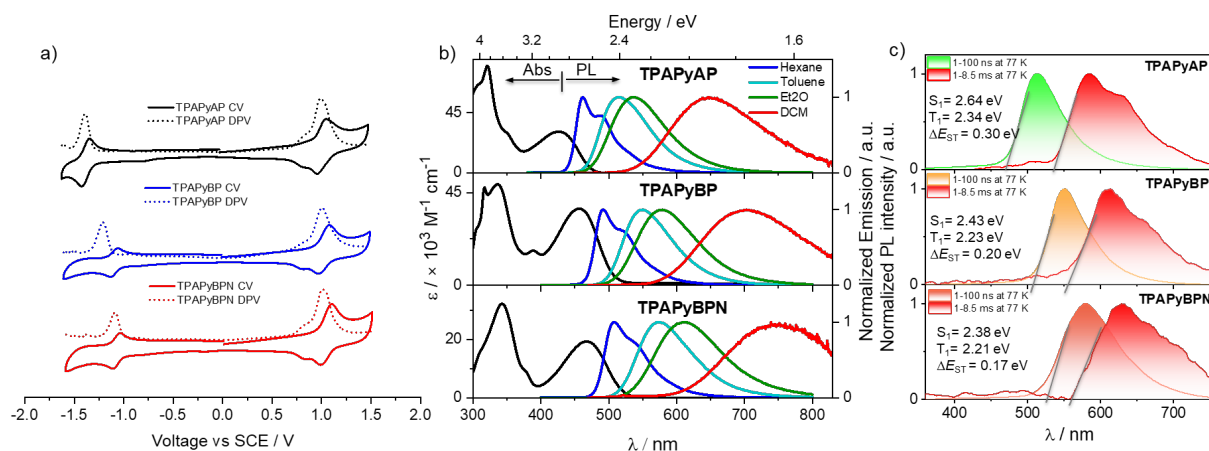
Figure 4. (a) CVs and DPVs measured in degassed DCM with 0.1 M [^{n}Bu$_4$N]PF$_6$ as the supporting electrolyte and Fc/Fc$^+$ as the internal reference (0.46 V vs SCE).[46] Scan rate = 100 mV s^{-1}; (b) UV-vis absorption and PL solvatochromism study (λ_{exc} = 340 nm, Et2O= diethyl ether, DCM = dichloromethane); (c) prompt fluorescence and phosphorescence spectra of **TPAPyAP**, **TPAPyBP** and **TPAPyBPN** toluene at 77 K (λ_{exc} = 343 nm, prompt and delayed fluorescence spectra were acquired across a 1–100 ns and a 1–8.5 ms time range, respectively).

Photophysical properties in solution

The UV-Vis absorption spectra of the three emitters in dilute toluene are shown in Figure **4b** and the photophysical properties are summarized in Table **1**. All three compounds exhibit strong absorption bands at around 320 nm, which are assigned to locally excited (LE) π–π* transitions of the donors and acceptor moieties based on the TD-DFT predicted transitions (Figure **S19**). A strong and broad absorption band is observed at 427 nm (ε = 31×10^3 M^{-1}cm^{-1}) for **TPAPyAP**, 456 nm (ε = 37×10^3 M^{-1}cm^{-1}) for **TPAPyBP** and 469 nm (ε = 19 ×10^3 M^{-1}cm^{-1}) for **TPAPyBPN**, which is assigned in each case to an intramolecular charge transfer (ICT) transition from the TPA donor to the acceptor moiety. The molar absorption coefficient of the ICT band at 427 nm of **TPAPyAP** is higher than that of ICT band at 469 nm of **TPAPyBPN**, which aligns with the TD-DFT calculated oscillator strength (f = 0.47 for **TPAPyAP** and f =0.36 for **TPAPyBPN**, Figure **3b**), while **TPAPyBP** exhibits the highest ε at 456 nm (f of 0.39). The ICT absorption bands of these three compounds also expectedly shift to lower energies as the acceptor strength increases. All compounds show unstructured and broad PL spectra in toluene (Figure **3b**), indicative of an excited

13

state of ICT character, with peak maxima, λ_{PL}, at 513 nm, 550 nm, and 575 nm for **TPAPyAP,** **TPAPyBP** and **TPAPyBPN**, respectively. Positive solvatochromism is observed for all three compounds (Figure **4b**, Table **S4**), which is consistent with the ICT nature of the emissive excited state. The optical bandgaps, E_g, calculated from the intersection point of the normalized absorption and emission spectra, are 2.62 eV, 2.46 eV, and 2.38 eV for **TPAPyAP, TPAPyBP** and **TPAPyBPN**, respectively (Figure **S20**). The photoluminescence quantum yields, Φ_{PL}, in degassed toluene solution of **TPAPyAP, TPAPyBP** and **TPAPyBPN** are 93, 89, and 86%, respectively, decreasing to 85, 81, and 78% upon exposure to oxygen (Table **1**).

The PL decays of the three emitters in toluene under degassed and aerated conditions were measured using time-correlated single-photon counting (TCSPC, Figure **S21**). There is only a single decay component (monoexponential) observed for all three compounds, with lifetimes, τ_p, of 4.6 ns for **TPAPyAP,** 5.6 ns for **TPAPyBP** and 7.2 ns for **TPAPyBPN**. While there is no long-lived TADF emission observed, this may be completely quenched by nonradiative decay in solution; a phenomenon shown in some previously reported TADF compounds, especially for TPA-based TADF emitters.[47–50] The S_1 and T_1 energies of the three emitters were elucidated from the onsets of the respective fluorescence and phosphorescence spectra determined in frozen toluene at 77 K (Figure **4c**, Table **1**). The S_1 energies of **TPAPyAP, TPAPyBP** and **TPAPyBPN**, are 2.64 eV, 2.43 eV, and 2.38 eV, while the T_1 energies are 2.34 eV, 2.23 eV, and 2.21 eV, respectively. The phosphorescence spectra of all three compounds are structured, and each is assigned from the TDA-DFT calculations as a mixed locally excited triplet (^{3}LE) state of the acceptor and ^{3}ICT state (Figure **3**). The ΔE_{ST} values of **TPAPyAP, TPAPyBP** and **TPAPyBPN** are 0.30 eV, 0.20 and 0.17 eV, respectively, which, though smaller than the calculated values, nonetheless mirror the trend predicted from the theoretical study. Similar to the other TPA-based TADF emitters,[48,51] these three compounds also have large ΔE_{ST} in solution, yet TADF is observed in the solid state.

Fluorescence sensing of Lewis acids

Recognizing that the acceptors contain Lewis basic nitrogen atoms of differing number and strength and we decided to assess the potential of these compounds to act as selective optical sensors of Lewis acids. Although TADF luminophores have shown great potential as sensors,[23,52]

such as for oxygen, [53–55] as temperature probes, [27,29,56] and for acid–base sensing.[57] There is to date no report on the use of TADF luminophores for Lewis acid sensing. We first investigated the optical sensing responses of **TPAPyBP** (1.3×10^{-4} M) towards different metal ions. There is a quenching of the PL intensity of **TPAPyBP** at 550 nm with varying degrees of efficiency upon addition of excess of various metal salts ($NaCl$, $NiCl_2$, $Ni(OAc)_2$, CuI, $Cu(OAc)_2$, $CoCl_2$, $CuCl$, $CuCl_2$, $ZnCl_2$, $SnCl_2$, $Zn(BF_4)_2$, $FeCl_3$, and $AlCl_3$) in an ethanol/toluene(1/99, *v/v*) solvent mixture Figure **5a** and **e**). Remarkably, the emission responses upon addition of $ZnCl_2$ and $SnCl_2$ are particularly distinct, as in both cases there are the emergence of new, strong emission bands at around 680 nm (Figure **5b** and **c**). However, it is noteworthy that only the addition of $ZnCl_2$ to the **TPAPyBP** toluene solution resulted in a distinct intense red emission. As shown in Figure **5d**, new, strong absorption bands were observed for $ZnCl_2$, $SnCl_2$, $Zn(BF_4)_2$, $FeCl_3$ and $AlCl_3$. Similarly, the spectral response of **TPAPyAP** and **TPAPyBPN** also revealed a binding selectivity towards $ZnCl_2$, showing a new, red-shifted emission band at 650 nm and 655 nm, respectively (Figure **S22**). The Job plot for both compounds indicates the same 1:1 binding stoichiometry as that observed for **TPAPyBP** (Figure **S22**). Given the more distinct and stronger optical response using **TPAPyBP** compared to **TPAPyAP** and **TPAPyBPN**, here we only focused on **TPAPyBP**.
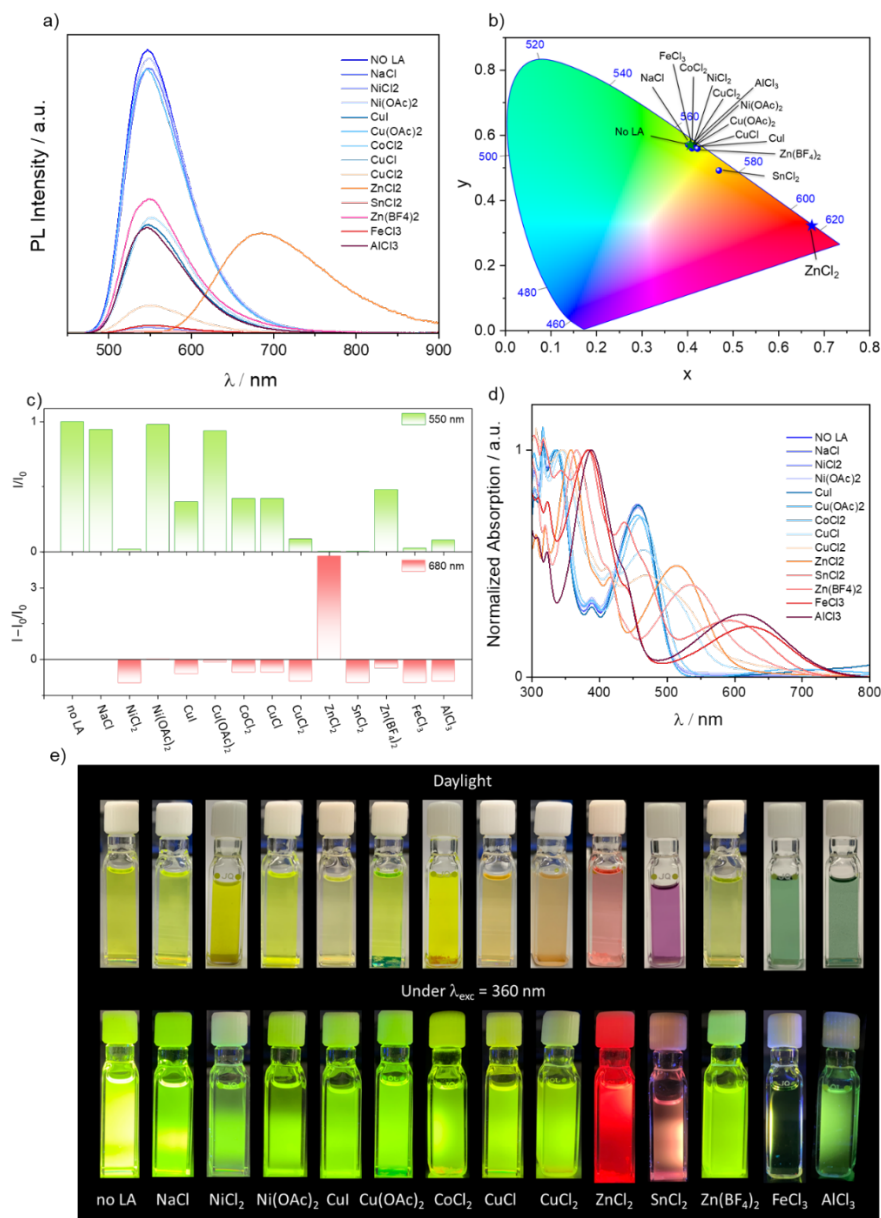
Figure **5.** (a) PL measurements of **TPAPyBP** (1.3×10^{-4} M) with different metal salts (10 equiv.); (b) The related CIE diagram; (c) Variation of the PL intensity at 550 nm and 680 nm (λ_{exc} = 410 nm) of **TPAPyBP** (0.1 μM) in the presence of 10 equiv. of metal salt [ethanol/toluene (1/99, v/v)]; (d) Absorption measurements of 0.1 μM **TPAPyBP** with different metal salts (10 equiv.) (e) Samples in daylight and excited by UV torch (λ_{exc} = 360 nm) of **TPAPyBP** upon addition of 10 equiv. of different metal salt (mixture of ethanol and toluene).

16

The intriguing observation of this selective $ZnCl_2$ sensing prompted us to explore the underlying mechanism. We first investigated the detection limit of $ZnCl_2$, which is correlated with the concentration of the emitter. As shown in Figure **S23**, the fluorescence spectra of different concentrations of **TPAPyBP** in a mixture of ethanol and toluene (0.0012/1 v/v) upon addition of 1 equivalent of $ZnCl_2$ were measured. As the concentration of **TPAPyBP**:$ZnCl_2$ (1:1 equiv.) increases, the fluorescence intensity at 555 nm increases until the concentration reaches 1.3×10^{-5} M. When the concentration increases further, the intensity of 555 nm emission band decreases while concomitantly a new emission band at 680 nm emerges and gradually becomes the principal emission band, reflecting the observed color change from green to deep red (Figure **S23c** and **e**). As expected, the corresponding absorption spectrum exhibits a new band at 505 nm, which increases in intensity as the concentration of **TPAPyBP**:$ZnCl_2$ (1:1 equiv.) increases. As shown in Figure **S23f**, the detection limit of $ZnCl_2$ is around 5.0×10^{-5} M: at this concentration, the presence of the 1:1 adduct with **TPAPyBP** can be confirmed. Furthermore, we highlight the fast reaction time, which occurs within several seconds (ESI Video 1). This rapid response is highly desirable for sensing applications.

We then systematically investigated the PL response of **TPAPyBP** (1.3×10^{-4} M) in toluene upon gradual addition of $ZnCl_2$ (0.10 M) in ethanol. As shown in Figure **6a-c**, the PL intensity of **TPAPyBP** at 550 nm decreases progressively upon addition of $ZnCl_2$ with concomitant increase of a new emission band at 680 nm. This leads to a stark spectral response where the emission changes from greenish yellow to deep-red Figure **6b**, with corresponding the Commission International de L'Éclairage (CIE) coordinates from (0.44, 0.55) to (0.61, 0.38), Figure **6c**. The time-resolved photoluminescence (TRPL) of **TPAPyBP** with 10 equiv. of $ZnCl_2$ still shows monoexponential decay kinetics; however, the lifetime is shorter at 2.9 ns compared to 4.9 ns in the absence of $ZnCl_2$ (Figure **S24**). Similarly, there are distinct spectral changes in the UV/vis absorption spectrum whereupon gradual addition of $ZnCl_2$, the absorption band at 338 nm was bathochromically shifted to 358 nm while a new CT band appeared at 505 nm, probably due to the formation of a Zn complex (Figure **6d**). An isosbestic point at 487 nm and the 1:1 stoichiometry identified in the Job plot indicates that only a single $ZnCl_2$ is coordinated to **TPAPyBP** (Figure **6e**). Single crystals were grown by slow evaporation of a saturated toluene solution of the complex at room temperature. The structure of **Zn(TPAPyBP)Cl₂** is shown in Figure **6f** and reveals that

the Zinc ion adopts a distorted tetrahedral geometry, coordinated through the pyridyl nitrogen of **TPAPyBP** (N1), two chlorido ligands and a molecule of ethanol solvent (N-Zn-Cl bond angle of 107.6(2) and 116.0(2)º and N-Zn-O bond angle of 96.5(2)º). This, or a structurally related tetrahedral complex, is the likely putative species in solution. The ^{1}H NMR spectrum of **TPAPyBP** with increasing concertation of $ZnCl_2$ in $CDCl_3$ revealed that the resonances at positions 1 and 3 (Figure **S25**) of **TPAPyBP** were the most perturbed upon addition of $ZnCl_2$, suggesting a possible coordination of Zn^{2+} ion through pyrido[3,4-b]pyrazine core of the acceptor (Figure **6f**). Furthermore, HRMS of **TPAPyBP** with excess $ZnCl_2$ confirms the formation of a complex with a 1:1 stoichiometry (Figure **S26**).

For more insights into the origin of new deep red emission in solution, the HOMOs and LUMOs of **TPAPyBP** and **Zn(TPAPyBP)Cl₂** calculated at the PBE0/6-31G(d,p) level (based on the structure obtained from the single crystal X-ray diffraction study) are shown in Figure **6f**. The energy levels of both the LUMO (–2.82 eV) and the HOMO (–5.63 eV) for **Zn(TPAPyBP)Cl₂** are significantly stabilized compared to those of **TPAPyBP** (LUMO: –2.40 eV, HOMO: –5.35 eV), leading to a decrease in the $\Delta E_{HOMO-LUMO}$ from 2.95 eV to 2.81 eV (Figure **6g**). As excepted, the S_1 energy decreases to 2.38 eV for **Zn(TPAPyBP)Cl₂** from 2.55 eV of **TPAPyBP**, corresponding to a large red-shift of both the CT band of the absorption and the emission of **TPAPyBP** upon addition of $ZnCl_2$ (Figure **5**).
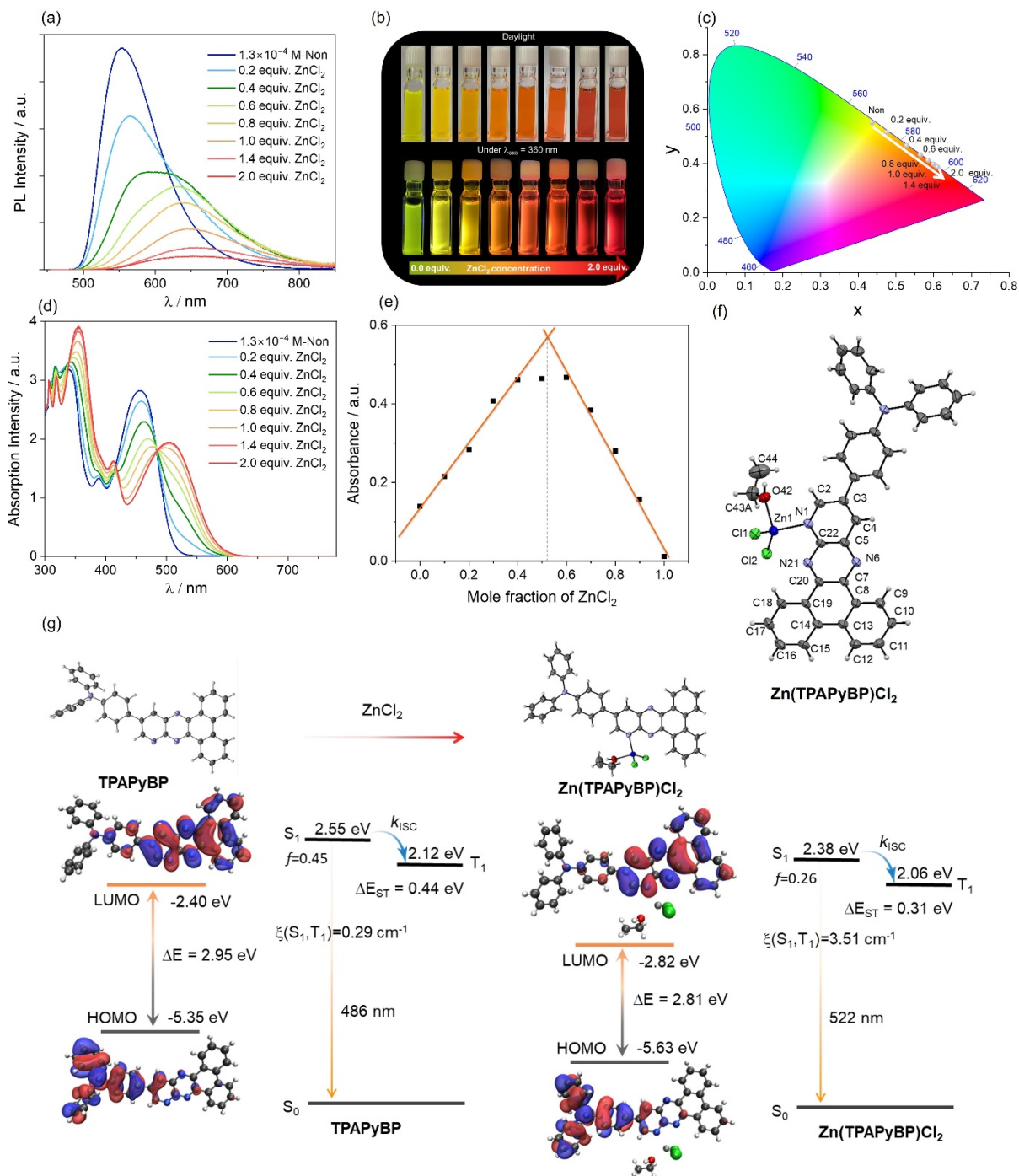
18

Figure 6. (a) PL measurements of **TPAPyBP** ($1.3×10^{-4}$ M) with the addition of $ZnCl_2$ from 0 to 2.0 equiv. (λ_{exc} = 487 nm); (b) Samples in daylight and excited by UV torch (λ_{exc} = 360 nm) of **TPAPyBP** $ZnCl_2$ from 0 to 2.0 equiv.; (c) The corresponding CIE coordinates of **TPAPyBP** ($1.3×10^{-4}$ M) with the addition of $ZnCl_2$ from 0 to 2.0 equiv.; (d) UV−Vis absorption spectra obtained from **TPAPyBP** ($1.3×10^{-4}$ M) with the addition of $ZnCl_2$ from 0 to 2.0 equiv.; (e) Job plot

19

of absorbance (λ_{abs} = 510 nm) for the determination of binding stoichiometry between **TPAPyBP** and $ZnCl_2$. (f) Thermal ellipsoid plot of the single crystal structure of **Zn(TPAPyBP)Cl₂** with partial atomic numbering (Ellipsoids are drawn at the 50% probability level, toluene solvent and minor component of disorder in the coordinated EtOH are omitted) (g) Combined view of the single crystal structures of **TPAPyBP** and **Zn(TPAPyBP)Cl₂**, and the corresponding frontier molecular orbitals (isovalue: 0.02) calculated using single crystal geometry in the gas phase at the PBE0/6-31G(d,p) level.

Photophysical properties in the solid state

We next measured the photophysical properties of all three compounds in an OLED-relevant nonpolar host (4,4′-bis(*N*-carbazolyl)-1,1′-biphenyl (CBP)) at different weight concentrations ranging from 2 to 10 wt% (Figure **S27**). The 2 wt% doped CBP films of **TPAPyAP, TPAPyBP** and **TPAPyBPN** emit at λ_{PL} of 537, 560 and 585 nm, respectively, corresponding to the emission in dilute toluene solutions. The Φ_{PL} of the 2 wt% CBP doped films of **TPAPyAP TPAPyBP** and **TPAPyBPN** are 62, 60 and 62%, respectively (Table **S5**). As the doping concentration increased, all compounds showed a red-shifted emission accompanied by a decrease in Φ_{PL}. While the 10 wt% **TPAPyBPN** doped film in CBP exhibited a more pronounced red-shifted emission at λ_{PL} of 605 nm and a high Φ_{PL} of 56%; thus, this doping concentration was chosen for the following characterization studies. As shown in Figure **S27**, all three compounds show unstructured ICT-based emission at room temperature. Similar to that observed in toluene at 77 K, the prompt fluorescence of 2 wt% **TPAPyAP**, **TPAPyBP** and **TPAPyBPN** doped in CBP film at 77 K are structureless, with associated S_1 energies of 2.50, 2.33 and 2.23 eV, respectively. As expected, the phosphorescence spectra of all three compounds are structured, with T_1 values of 2.18, 2.18 and 2.17 eV, matching well with the TDA-DFT calculations as a mixed ^{3}LE/ICT state. The ΔE_{ST} of these films of **TPAPyAP, TPAPyBP** and **TPAPyBPN** are 0.32 eV, 0.15 and 0.06 eV, respectively (Figure **S27b**). As shown in Figure **S28**, **TPAPyBP** and **TPAPyBPN** each showed multiexponential decay kinetics at room temperature, with average prompt fluorescence lifetimes, τ_p, of 10.0 ns and 15.0 ns, respectively (Figure **S28**), and average delayed emission lifetimes, τ_d, of 2.3 ms and 2.1 ms, respectively. The relative intensity of the delayed PL increases with increasing temperature from 100 K to 300 K for both compounds, thereby corroborating the TADF

20

nature of the emission of these three compounds in the CBP films. However, **TPAPyAP** showed monoexponential decay kinetics with a fluorescence lifetime of 8.4 ns (Figure **S28a**), which can be explained by the large ΔE_{ST} and inefficient TADF in the doped CBP film. We also explored the photophysical properties of the three emitters in a higher polarity host, PPT (Figure **S29**). **TPAPyBPN** exhibited the most red-shifted emission of 53 nm compared to that in **TPAPyAP** (42 nm) and **TPAPyAP** (48 nm). The larger red-shift in **TPAPyBPN** can be attributed to it having the largest dipole moment of 5.7 D. The Φ_{PL} values of **TPAPyAP, TPAPyBP** and **TPAPyBPN** doped in nonpolar CBP are 62, 60 and 62%, respectively, and they remain high, at 75, 63 and 60 %, in polar PPT, respectively in 2 wt% doped films (Table **S5**). As shown in Figure **S30,** the doped PPT films of **TPAPyAP, TPAPyBP** and **TPAPyBPN** all show multiexponential decay kinetics with average τ_p of 6.8 ns, 9.7 ns, and 14.0 ns and average τ_d of 1.4 ms, 0.68 ms and 0.11 ms at room temperature, respectively. Temperature-dependent time-resolved PL decays evidence the TADF nature of the emission in the PPT doped films (Figure **S30**). The S_1 levels of **TPAPyAP**, **TPAPyBP** and **TPAPyBPN** are stabilized modestly from 2.48 to 2.41 eV, 2.33 to 2.31 eV, 2.22 to 2.11 eV, respectively, in PPT host compared to that in CBP host. The corresponding ΔE_{ST} values decrease (Table **1**, Figure **S31**), leading to a shorter τ_d in PPT than in CBP.

Table **1**. Photophysical properties of **TPAPyAP, TPAPyBP**, **and TPAPyBPN** in solution and the solid state.

	λ_{PL}[a] / nm	τ_p[a] / ns	τ_d / ms	S_1/T_1 [b] / eV	ΔE_{ST} / eV	Φ_{PL}[c] /%
in solution						
TPAPyAP	516	4.6	-	2.64/2.34	0.30	93 (85)
TPAPyBP	550	5.6	-	2.43/2.23	0.20	89 (81)
TPAPyBPN	575	7.2	-	2.38/2.21	0.17	86 (78)
in CBP[d]						
TPAPyAP (2 wt%)	537	8.4	-	2.50/2.18	0.32	62 (61)
TPAPyBP (2 wt%)	559	10.0	2.3	2.33/2.18	0.15	60 (58)
TPAPyBPN (10 wt%)	605	15.0	2.1	2.23/2.17	0.06	56 (53)
in PPT[d]						
TPAPyAP (2 wt%)	584	6.8	1.42	2.41/2.33	0.11	75 (70)
TPAPyBP (2 wt%)	624	9.7	0.61	2.31/2.28	0.03	63 (58)
TPAPyBPN (10 wt%)	675	14.0	0.11	2.12/2.11	0.01	57 (47)

21

OLEDs

We next proceeded to fabricate vacuum-deposited bottom-emitting OLED devices using **TPAPyAP**, **TPAPyBP** and **TPAPyBPN** as emitters. As shown in Figure **7a**, we fabricated OLEDs with two different device architectures that differ in terms of the host matrix used in the emissive layer (EML): CBP (device **A**); and PPT (device **B**). As shown in Figure **7a**, the general device architecture consists of indium-tin-oxide (ITO)/ 1,4,5,8,9,11-hexaazatriphenylenehexacarbonitrile (HATCN) (5 nm)/ 1,1-bis[(di-4-tolylamino)phenyl]cyclohexane (TAPC) (40 nm)/tris(4-carbazoyl-9-ylphenyl)amine (TCTA) (10 nm)/ 1,3-bis(*N*-carbazolyl)benzene (mCP) (10 nm)/EML (20 or 35 nm)/ 1,3,5-tri[(3-pyridyl)-phen-3-yl]benzene (TmPyPB) (50 or 70 nm)/ LiF (0.8 nm)/ Al (100 nm). Here, HATCN was used as a layer for hole injection (HIL), TAPC and TCTA play the role in hole transporting layers (HTL), mCP acts as an electron blocking layer (EBL), TmPyPB acts as both an electron transport layer (ETL) and a hole blocking layer (HBL) due to its deep HOMO (-6.7 eV),[59] and LiF acts as an electron injection layer (EIL) by modifying the work function of the aluminum cathode. Device **A** consisted of a 20 nm EML comprising 2 wt% of **TPAPyAP**, 2 wt% **TPAPyBP** or 10 wt% of **TPAPyBPN** doped into CBP and a 50 nm thick TmPyPB layer, while device **B** consisted of a 35 nm thick EML of 10 wt% **TPAPyBPN** doped in PPT and a 70 nm thick TmPyPB layer. The molecular structures of the materials used in both devices are shown in Figure **7b**.
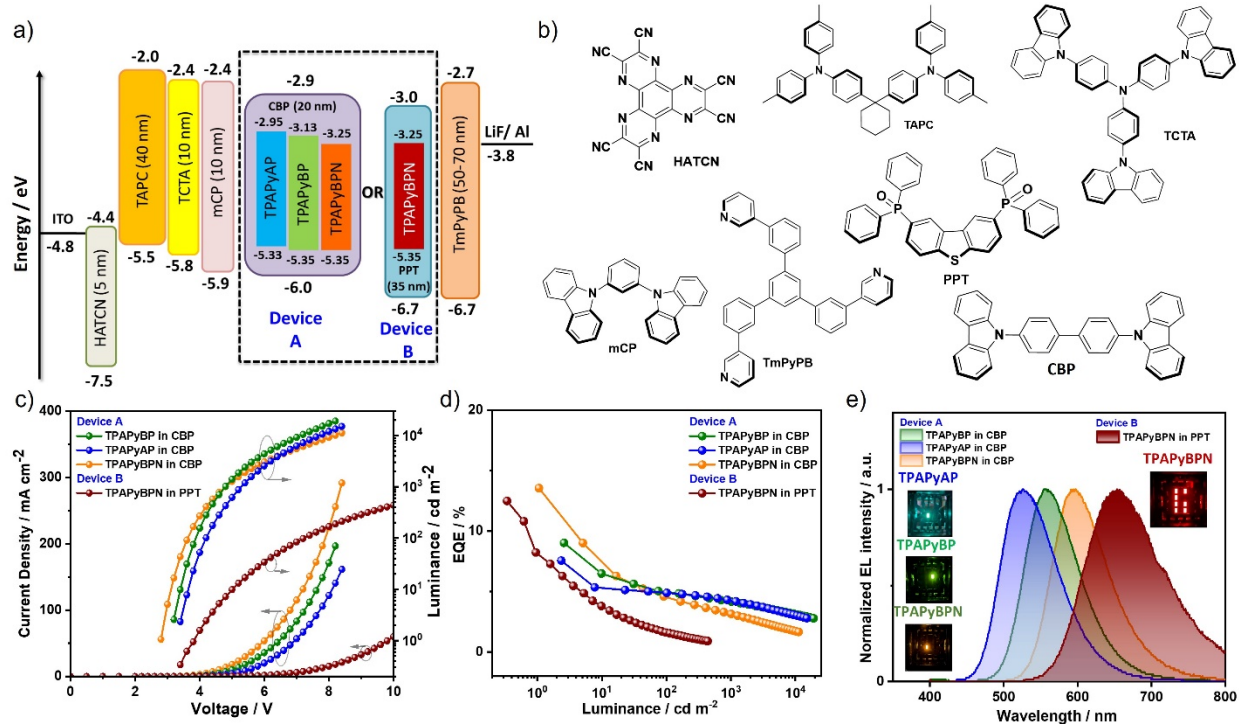
Figure **7**. (a) Energy level diagram of materials employed in the devices with device **A**: ITO/ HATCN (5nm)/ TAPC (40nm)/ TCTA (10 nm)/ mCP (10 nm)/ EML:CBP (20 nm)/ TmPYPB (50 nm)/ LiF (0.8 nm)/ Al (100 nm) and device **B**: ITO/ HATCN (5nm)/ TAPC (40nm)/ TCTA (10 nm)/ mCP (10 nm)/ **TPAPyBPN**:PPT (35 nm)/ TmPyPB (70 nm)/ LiF (0.8 nm)/ Al (100 nm); (b) Molecular structure of materials used in the devices; (c) Current density and luminance versus voltage characteristics for the devices; (d) External quantum efficiency versus luminance curves for the devices; (e) Electroluminescence spectra of the device, the inset is the electroluminescence of **TPAPyAP**, **TPAPyBP** and **TPAPyBPN** in CBP and **TPAPyBPN** in PPT.

The performance of the OLEDs is summarized in Table **2**. The EQE–luminance, current density–voltage–luminance (J–V–L) curves, and electroluminescence spectra (EL) are given in Figures **7c-e**. Initially, we fabricated devices using device structure **A** and observed that each EL spectrum is similar to that of the corresponding PL spectrum in the CBP doped thin film, with EL maxima, λ_{EL}, of 526 nm for **TPAPyAP**, 558 nm for **TPAPyBP** and 597 nm for **TPAPyBPN**, with corresponding Commission International de l'Éclairage, CIE, coordinates of (0.317, 0.578), (0.434, 0.547) and (0.565, 0.433), respectively (Figure **7e**). The EQE$_{max}$ of the **TPAPyAP**-based

device is 7.6% while that of the **TPAPyBP**-based device is 9.1% and that of the **TPAPyBPN-** based device is 13.6% (Table **2** and Figures **S32** and **S33**). Devices of **TPAPyAP** and **TPAPyBP** showed similar, moderate efficiency roll-off, with the EQE at 100 cd/m^2 (EQE$_{100}$) at 4.9%, and the EQE at 1,000 cd/m^2 (EQE$_{1000}$) at 4.3%; however, the **TPAPyBPN**-based device showed a more severe efficiency roll-off with EQE$_{100}$ at 4.6% and EQE$_{1000}$ at 3.2%. The theoretical EQE$_{max}$ is 13.9% for **TPAPyBPN** in CBP when considering an outcoupling efficiency of $\chi_{out} \approx 25\%$ that assumes that the film is isotropic. We next fabricated device **B** with an EML containing **TPAPyBPN** doped into the PPT host at the same 10 wt% doping concentration as that in CBP. As expected, the λ_{EL} is red-shifted to 657 nm [CIE coordinates (0.651, 0.348)], close to the λ_{PL} for the 10 wt% doped film in PPT (Figure **S29**). The EQE$_{max}$ of **TPAPyBPN**-based device **B** was 12.5%, close to that for the **TPAPyBPN**-based device **A** (in CBP) and is also close to the theoretical EQE$_{max}$ = 14.2%. However, the **TPAPyBPN**-based device **B** showed much higher efficiency roll-off, despite the short τ_d and small ΔE_{ST} of the **TPAPyBPN** doped film in PPT.

Table **2**. Electroluminescence data for the devices[a]

Emitter	Host	V_{on}[c] / V	λ_{EL}[d] / nm	CE_{max} / cd A^{-1}	PE_{max} / lm W^{-1}	EQE[e] / %	CIE[d] / x,y
TPAPyAP[a]	CBP (2.0%)	3.4	526	25.24	23.35	7.6/4.9/4.3	0.317, 0.578
TPAPyBP[a]	CBP (2.0%)	3.2	558	31.57	29.17	9.1/4.9/4.3	0.434, 0.547
TPAPyBPN[a]	CBP (10%)	2.8	596	31.52	35.36	13.6/4.6/3.2	0.565, 0.433
TPAPyBPN[b]	PPT (10%)	3.4	657	10.14	9.4	12.5/1.6/-	0.651, 0.348

[a] Device structure **A**: ITO/ HATCN (5nm)/ TAPC (40nm)/ TCTA (10 nm)/ mCP (10 nm)/ EML:CBP (20 nm)/ TmPyPB (50 nm)/ LiF (0.8 nm)/ Al (100 nm). [b] Device structure **B**: ITO/ HATCN (5nm)/ TAPC (40nm)/ TCTA (10 nm)/ mCP (10 nm)/ **TPAPyBPN**:PPT (35 nm)/ TmPyPB (70 nm)/ LiF (0.8 nm)/ Al (100 nm). [c] The turn-on voltage at EQE$_{max}$. [d] The electroluminescence maximum and CIE recorded at 6 V. [e] EQE$_{max}$/EQE$_{100}$/ EQE$_{1000}$.

Conclusions

A family of TPA derivatives, **TPAPyAP**, **TPAPyBP** and **TPAPyBPN**, shows progressively red-shifted emission in toluene as a function of the increasing number of nitrogen atoms in the heterocyclic pyrazine-based acceptors. All three compounds exhibit a spectral response to the detection of $ZnCl_2$ in toluene, with the most notable being for **TPAPyBP**, where the emission rapidly changed from green (λ_{PL}=550 nm) to deep red (λ_{PL}=680 nm), which is distinct from the typical response of most Zn^{2+} or $ZnCl_2$ sensors that only rely on changes in emission intensity. We also investigated the potential of these compounds as emitters in OLEDs. Both **TPAPyBP** and **TPAPyBPN** emit in the deep red in PPT, while **TPAPyAP** exhibits a smaller red-shift from green emission in CBP to yellow emission in PPT compared to the other two compounds. The OLEDs showed moderate efficiencies, with the device with **TPAPyBPN** doped in PPT emitting at λ_{EL}= 657 nm and showing an EQE_{max} 12.5%. This electroluminescence was red-shifted by 61 nm compared to device the with CBP as the host (λ_{EL}= 596 nm, EQE_{max} = 13.6%), a reflection of the impact of solid-state solvatochromism.
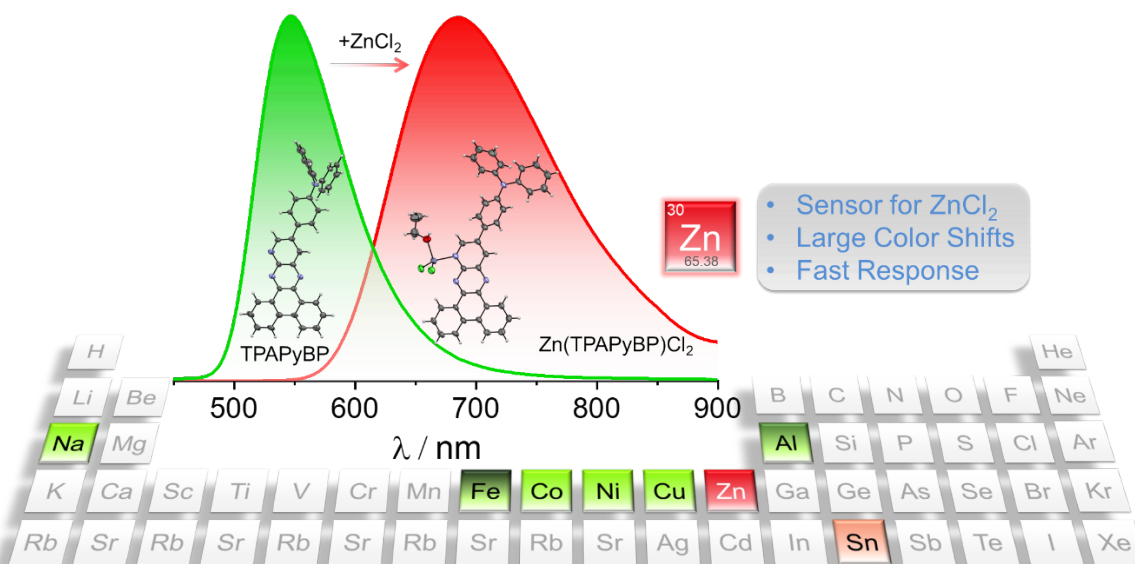
Conflict of Interest

The authors declare no conflict of interest.

Supporting Information

^{1}H and ^{13}C NMR spectra, HRMS, EA and HPLC of all target compounds; X-ray crystallographic data; supplementary computational data; supplementary photophysical data.

TOC Graphic

References

[1]   A. Steinegger, O. S. Wolfbeis, S. M. Borisov, *Chem. Rev.* **2020**, *120*, 12357.

[2]   K. T. V Grattan, T. Sun, *Sensors Actuators A Phys.* **2000**, *82*, 40.

[3]   X. Yan, H. Li, X. Su, *TrAC Trends Anal. Chem.* **2018**, *103*, 1.

[4]   N. Sabri, S. A. Aljunid, M. S. Salim, R. B. Ahmad, R. Kamaruddin, *J. Phys. Conf. Ser.* **2013**, *423*, 012064.

[5]   M. Vendrell, D. Zhai, J. C. Er, Y.-T. Chang, *Chem. Rev.* **2012**, *112*, 4391.

[6]   L. Basabe-Desmonts, D. N. Reinhoudt, M. Crego-Calama, *Chem. Soc. Rev.* **2007**, *36*, 993.

[7]   A. P. Demchenko, *Introduction to fluorescence sensing*, Springer Science & Business Media, **2008**.

[8]   H. N. Kim, M. H. Lee, H. J. Kim, J. S. Kim, J. Yoon, *Chem. Soc. Rev.* **2008**, *37*, 1465.

[9]   Y. Wang, X. Wang, W. Ma, R. Lu, W. Zhou, H. Gao, *Chemosensors* **2022**, *10*, 399.

[10]   B. Sam, L. George, A. Varghese, *J. Fluoresc.* **2021**, *31*, 1251.

[11]   X. Chen, T. Pradhan, F. Wang, J. S. Kim, J. Yoon, *Chem. Rev.* **2012**, *112*, 1910.

[12]   M. Poddar, R. Misra, *Coord. Chem. Rev.* **2020**, *421*, 213462.

[13]   A. Loudet, K. Burgess, *Chem. Rev.* **2007**, *107*, 4891.

[14]   N. Roy, A. Dutta, P. Mondal, P. C. Paul, T. Sanjoy Singh, *J. Fluoresc.* **2017**, *27*, 1307.

[15]   S. M. Borisov, G. Zenkl, I. Klimant, *ACS Appl. Mater. Interfaces* **2010**, *2*, 366.

[16]   Y. You, S. Cho, W. Nam, *Inorg. Chem.* **2014**, *53*, 1804.

[17]   Q. Zhao, F. Li, C. Huang, *Chem. Soc. Rev.* **2010**, *39*, 3007.

[18]   M. Han, Y. Tian, Z. Yuan, L. Zhu, B. Ma, *Angew. Chemie Int. Ed.* **2014**, *53*, 10908.

[19]   H. Uoyama, K. Goushi, K. Shizu, H. Nomura, C. Adachi, *Nature* **2012**, *492*, 234.

[20]   M. Y. Wong, E. Zysman-Colman, *Adv. Mater.* **2017**, *29*, 1605444.

[21] D. Sun, C. Si, T. Wang, E. Zysman-Colman, *Adv. Photonics Res.* **2022**, 2200203.

[22] M. A. Bryden, E. Zysman-Colman, *Chem. Soc. Rev.* **2021**, *50*, 7587.

[23] F. Ni, N. Li, L. Zhan, C. Yang, *Adv. Opt. Mater.* **2020**, *8*, 1.

[24] F. Fang, L. Zhu, M. Li, Y. Song, M. Sun, D. Zhao, J. Zhang, *Adv. Sci.* **2021**, *8*, 2102970.

[25] A. Russegger, L. Eiber, A. Steinegger, S. M. Borisov, *Chemosensors* **2022**, *10*, 91.

[26] S. Qiu, J. Yu, T. Zhou, K. Zhang, Y. Duan, X. Ban, Q. Zhu, L. Shi, D. Zhang, *Opt. Mater. (Amst).* **2021**, *119*, 111303.

[27] C. J. Christopherson, D. M. Mayder, J. Poisson, N. R. Paisley, C. M. Tonge, Z. M. Hudson, *ACS Appl. Mater. Interfaces* **2020**, *12*, 20000.

[28] J. C. Fister, D. Rank, J. M. Harris, *Anal. Chem.* **1995**, *67*, 4269.

[29] A. Steinegger, I. Klimant, S. M. Borisov, *Adv. Opt. Mater.* **2017**, *5*, 1.

[30] C. M. Tonge, N. R. Paisley, A. M. Polgar, K. Lix, W. R. Algar, Z. M. Hudson, *ACS Appl. Mater. Interfaces* **2020**, *12*, 6525.

[31] X. Li, G. Baryshnikov, C. Deng, X. Bao, B. Wu, Y. Zhou, H. Ågren, L. Zhu, *Nat. Commun.* **2019**, *10*, 731.

[32] H. Yin, Y. Wu, X. Peng, F. Song, *Chem. Commun.* **2020**, *56*, 10549.

[33] S. M. Wei, K. Feng, C. Li, N. Xie, Y. Wang, X. L. Yang, B. Chen, C. H. Tung, L. Z. Wu, *Matter* **2020**, *2*, 495.

[34] S. Madhav, A. Ahamad, P. Singh, P. K. Mishra, *Environ. Qual. Manag.* **2018**, *27*, 31.

[35] M. R. Rahimzadeh, M. R. Rahimzadeh, S. Kazemi, A. A. Moghadamnia, *Mini Rev. Med. Chem.* **2020**, *20*, 1489.

[36] P. P. Das, P. Mohanty, A. K. Barick, P. Mohapatra, B. R. Jali, *Trends Sci.* **2023**, *20*, 5005.

[37] F. Himo, Z. P. Demko, L. Noodleman, K. B. Sharpless, *J. Am. Chem. Soc.* **2003**, *125*, 9983.

[38] E. Manandhar, J. H. Broome, J. Myrick, W. Lagrone, P. J. Cragg, K. J. Wallace, *Chem. Commun.* **2011**, *47*, 8796.

[39] C. Sabarinathan, M. Karthikeyan, R. M. Murugappan, S. P. Anthony, B. Shankar, K. Parthasarathy, T. Arumuganathan, *New J. Chem.* **2021**, *45*, 5576.

[40] T. Ghosh, B. G. Maiya, A. Samanta, *Dalton Trans.* **2006**, 795.

[41] C. Adamo, V. Barone, *J. Chem. Phys.* **1999**, *110*, 6158.

[42] G. A. Petersson, T. G. Tensfeldt, J. A. Montgomery, *J. Chem. Phys.* **1991**, *94*, 6091.

[43] S. M. Kerwin, *J. Am. Chem. Soc.* **2010**, *132*, 2466.

[44] S. Hirata, M. Head-Gordon, *Chem. Phys. Lett.* **1999**, *314*, 291.

[45] S. Grimme, *Chem. Phys. Lett.* **1996**, *259*, 128.

[46] N. G. Connelly, W. E. Geiger, *Chem. Rev.* **1996**, *96*, 877.

[47] S. Wang, X. Yan, Z. Cheng, H. Zhang, Y. Liu, Y. Wang, *Angew. Chemie Int. Ed.* **2015**, *54*, 13068.

[48] Y. Y. Wang, Y. L. Zhang, K. Tong, L. Ding, J. Fan, L. S. Liao, *J. Mater. Chem. C* **2019**, *7*, 15301.

[49] C. Zhou, S. Xiao, M. Wang, W. Jiang, H. Liu, S. Zhang, B. Yang, *Front. Chem.* **2019**, *7*, 1.

[50] Y. L. Zhang, Q. Ran, Q. Wang, Y. Liu, C. Hänisch, S. Reineke, J. Fan, L. S. Liao, *Adv. Mater.* **2019**, *31*, 1902368.

[51] J. L. He, Y. Tang, K. Zhang, Y. Zhao, Y. C. Lin, C. K. Hsu, C. H. Chen, T. L. Chiu, J. H. Lee, C. K. Wang, C. C. Wu, J. Fan, *Mater. Horizons* **2022**, *9*, 772.

[52] N. R. Paisley, C. M. Tonge, Z. M. Hudson, *Front. Chem.* **2020**, *8*, 229.

[53] I. Danyliv, Y. Danyliv, R. Lytvyn, O. Bezvikonnyi, D. Volyniuk, J. Simokaitiene, K. Ivaniuk, U. Tsiko, A. Tomkeviciene, A. Dabulienė, E. Skuodis, P. Stakhira, J. V. Grazulevicius, *Dyes Pigm.* **2021**, *193*, 109493.

[54] U. Tsiko, O. Bezvikonnyi, G. Sych, R. Keruckiene, D. Volyniuk, J. Simokaitiene, I. Danyliv, Y. Danyliv, A. Bucinskas, X. Tan, J. V. Grazulevicius, *J. Adv. Res.* **2021**, *33*, 41.

[55] C. A. DeRosa, J. Samonina-Kosicka, Z. Fan, H. C. Hendargo, D. H. Weitzel, G. M. Palmer, C. L. Fraser, *Macromolecules* **2015**, *48*, 2967.

[56] A. Steinegger, S. M. Borisov, *ACS Omega* **2020**, *5*, 7729.

[57] A. K. Mazumdar, G. P. Nanda, N. Yadav, U. Deori, U. Acharyya, B. Sk, P. Rajamalli, *Beilstein J. Org. Chem.* **2022**, *18*, 1177.

[58] W. H. Melhuish, *J. Phys. Chem.* **1961**, *65*, 229.

[59] S. J. Su, T. Chiba, T. Takeda, J. Kido, *Adv. Mater.* **2008**, *20*, 2125.